Science of the Total Environment 948 (2024) 174821

Contents lists available at ScienceDirect

Science of the Total Environment

journal homepage: www.elsevier.com/locate/scitotenv

Impacts of land cover changes on summer surface ozone in China during 2000–2019

Yang Cao [a], Xu Yue [b,*], Hong Liao [b], Xuemei Wang [c], Yadong Lei [d], Hao Zhou [e]

[a] Jiangsu Nanjing Environmental Monitoring Center, Nanjing 210041, China
[b] Jiangsu Key Laboratory of Atmospheric Environment Monitoring and Pollution Control, Jiangsu Collaborative Innovation Center of Atmospheric Environment and Equipment Technology, School of Environmental Science and Engineering, Nanjing University of Information Science & Technology (NUIST), Nanjing 210044, China
[c] Institute for Environment and Climate Research, Jinan University, Guangzhou 511443, China
[d] State Key Laboratory of Severe Weather & Key Laboratory of Atmospheric Chemistry of CMA, Chinese Academy of Meteorological Sciences, Beijing 100081, China
[e] College of Meteorology and Oceanography, National University of Defense Technology, Changsha 410073, China

HIGHLIGHTS

- The LULCC is found to enhance O_3 with a maximum center of 1-2 ppbv in NCP but cause moderate reduction in the South.
- The LULCC-induced changes in isoprene emissions show stronger impacts than dry deposition in affecting the O_3 budget.
- The inconsistency is attributed to the background chemical regimes with positive O_3 changes over VOC-limited regions but negative changes in NO_x-limited regions.

GRAPHICAL ABSTRACT

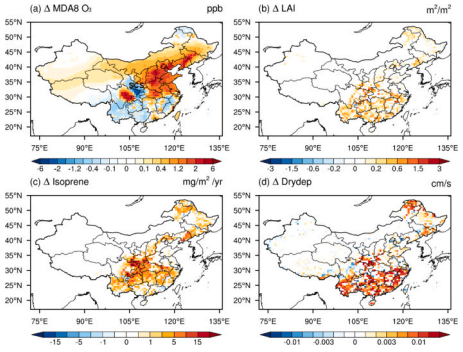

ARTICLE INFO

Editor: Meng Gao

Keywords:
Surface ozone
Land cover changes
Isoprene
Dry deposition
Forestation

ABSTRACT

China implemented continuous forestation and experienced significant greening tendency in the past several decades. While the ecological project brings benefits to regional carbon assimilation, it also affects surface ozone (O_3) pollution level through perturbations in biogenic emissions and dry deposition. Here, we use a coupled chemistry-vegetation model to assess the impacts of land use and land cover change (LULCC) on summertime surface O_3 in China during 2000–2019. The LULCC is found to enhance O_3 by 1–2 ppbv in already-polluted areas. In contrast, moderate reductions of −0.4 to −0.8 ppbv are predicted in southern China where the largest forest cover changes locate. Such inconsistency is attributed to the background chemical regimes with positive O_3 changes over VOC-limited regions but negative changes in NO_x-limited regions. The net contribution of LULCC to O_3 budget in China is 24.17 Kg/s, in which the positive contribution by more isoprene emissions almost triples the negative effects by the increased dry deposition. Although the LULCC-induced O_3 perturbation is much lower than the effects of anthropogenic emissions, forest expansion has exacerbated regional O_3 pollution in North China Plain and is expected to further enhance surface O_3 with continuous forestation in the future.

* Corresponding author.
E-mail address: yuexu@nuist.edu.cn (X. Yue).

https://doi.org/10.1016/j.scitotenv.2024.174821
Received 27 May 2024; Received in revised form 8 July 2024; Accepted 13 July 2024
Available online 16 July 2024

1. Introduction

Tropospheric ozone (O_3) is one of the detrimental air pollutants directly threatening human and ecosystem health (Monks et al., 2015). It is mainly generated through the reactions between nitrogen oxides ($NO_x = NO+NO_2$) and volatile organic compounds (VOCs) in the presence of sunlight, and is removed by dry/wet deposition and chemical reactions (Wang et al., 2020). Surface O_3 pollution is getting severe in China due to the fast industrialization and urbanization that generates a large amount of anthropogenic precursors (Li et al., 2019; Lu et al., 2018b). The maximum daily 8-h average O_3 (MDA8 O_3) concentration in 2016–2017 increased by about 20 % compared to 2013–2014, especially in North China Plain (NCP), Yangtze River Delta (YRD), and Pearl River Delta (PRD) (Lu et al., 2018a). Simulations also showed that summer MDA8 O_3 concentrations in China increased by ~1.9 ppbv/yr from 2013 to 2019, with meteorology contributing 0.7 ppbv/yr and anthropogenic emissions contributing 1.2 ppbv/yr (Li et al., 2020).The Clean Air Action (CAA) initiated at 2013 showed good effects in $PM_{2.5}$ control but failed to alleviate O_3 pollution (Chen et al., 2021; Zhai et al., 2019), even with the more stringent regulation of anthropogenic VOCs emissions after 2018 (Li et al., 2020). It is challenging to mitigate O_3 level due to its nonlinear dependence on precursors (Calfapietra et al., 2009) and the large contributions from the natural sources (Wang et al., 2011).

Both NO_x and VOCs can be emitted from natural systems. For NO_x, the lightning and soil are the top two natural sources, which are about 10 TgN yr^{-1} (Hudman et al., 2012; Vinken et al., 2014; Weng et al., 2020) but much smaller than the total of 30 TgN yr^{-1} from anthropogenic emissions (Huang et al., 2017; Vinken et al., 2014). In contrast, global biogenic VOCs (BVOCs) emissions are estimated to be 1150 TgC yr^{-1}, far exceeding the anthropogenic sources and accounting for >90 % of the total VOCs emissions (Guenther et al., 2012). Therefore, BVOCs (especially isoprene) are important precursors for O_3 generation even for the regions with large anthropogenic emissions. For example, Lu, et al. (Lu et al., 2019) estimated that BVOCs emissions contributed about 15 ppbv to the summer MDA8 O_3 concentrations in eastern China in 2016–2017. Mo et al. (2018) found that the isoprene emissions accounted for half of the total O_3 formation potential (OFP) during the summer noontime in Beijing. Zhang et al. (2017) pointed out that BVOCs contributed 10–19 % to O_3 concentrations during episode days in the United States. Meanwhile, surface O_3 can be removed through dry deposition, which is dominated by stomatal uptake over the vegetated land. Such process usually reaches the peak values around noontime and acts as an important sink of surface O_3 (Cao et al., 2022). Both the BVOCs emissions and the stomatal uptake are modulated by climatic conditions. The strong warming promotes BVOCs emissions and results in high level of O_3 pollution (Cao et al., 2021; Wang et al., 2019). Meanwhile, the drought conditions can inhibit stomatal conductance of vegetation, leading to the increase of surface O_3 concentrations (Lei et al., 2022).

In recent years, a significant greening tendency was observed in China (Chen et al., 2019; Yi et al., 2023). Such change is tightly related to the land use and land cover change (LULCC) following the national ecological projects (Yue et al., 2021). According to the inventory of the State Forestry Administration, China's forest coverage increased from 16 % in 1990 to 23 % in 2020 (http://www.forestry.gov.cn). While previous studies have examined the LULCC impacts on climate and environment, only a few have investigated contributions of LULCC to regional O_3 pollution in China (Table S1). Changes in forest coverage may perturb surface O_3 concentrations through both the BVOCs emissions (Chen et al., 2018) and the dry deposition (Gong et al., 2020). Ma et al. (2023) designed five parallel experiments with different LAI and land cover satellite datasets, finding that the relative difference exceeded 52 % in O_3 in central and eastern China. The result focused on the uncertainties of input database instead of continuous land cover changes. With the GEOS-Chem v9–02 model, Fu and Tai (2015) found that the LULCC caused a reduction of surface O_3 in most parts of East Asia during the summer of 1980–2010, mainly due to the enhanced dry deposition following the increased LAI. In contrast, Zhang et al. (2020) applied the WRF-Chem v3.7 model and revealed that LULCC increased surface O_3 by 1 % – 2 % in the metropolitans and 4 % – 5 % in the low-populated areas over the NCP. These studies explored the LULCC impacts in the earlier period before the establishment of air-quality monitoring network. As a result, the inadequate model validations led to the large uncertainties in their quantifications of LULCC effects. Furthermore, they mainly focused on the polluted regions in central China instead of the southern part where most of large-scale "greening" located (Wang et al., 2019). The impacts of LULCC on surface O_3 at the national scale for the recent decades remained unclear.

In this study, we explore the impacts of LULCC on surface O_3 pollution in China during the summer (June–August) of 2000–2019. We perform sensitivity experiments using the coupled chemistry-vegetation model GEOS-Chem-YIBs (Lei et al., 2020) to isolate the LULCC effects on BVOCs emissions and O_3 dry deposition. The global simulations with coarse resolution are performed to quantify the long-term trend of surface O_3 in China. Meanwhile, the regional simulations with fine resolution are conducted to better evaluate model performance and to understand the LULCC impacts on air pollution in recent years. For all simulations, we implement annually varied land cover data into the model, which dynamically predicts leaf area index (LAI) so as to affect both the BVOCs emissions and O_3 dry deposition.

2. Method and data

2.1. GEOS-Chem-YIBs model

We use the coupled chemistry-vegetation model GEOS-Chem-YIBs to simulate O_3 changes in China. GEOS-Chem is a global 3-D chemical transport model with the well-established NO_x-O_x-hydrocarbon-aerosol chemistry mechanism for gas-phase pollutants and aerosols (Park et al., 2004). The model is driven with meteorological forcing from the Modern-Era Retrospective analysis for Research and Application version 2 (MERRA2) (Rienecker et al., 2011). The emissions from different sources, regions, and species are calculated from the combinations of various inventories through the online Harvard–NASA Emissions Component (HEMCO) module (Keller et al., 2014; Lin et al., 2021). Anthropogenic emissions are adopted from the Community Emissions Data System (CEDS) for global domain (Hoesly et al., 2018). The MIX inventory for Asian domain (Li et al., 2017b), and the Multi-resolution Emission Inventory for China (MEIC) within Chinese domain (Li et al., 2017a; Zheng et al., 2018).

The Yale Interactive terrestrial Biosphere (YIBs) model is a well-evaluated vegetation model. The model can dynamically predict LAI and tree height based on vegetation photosynthesis and carbon allocation for nine plant functional types (PFTs), including evergreen needleleaf forest (ENF), deciduous broadleaf forest (DBF), evergreen broadleaf forest (EBF), shrubland, tundra, C_3/C_4 grasses, and C_3/C_4 crops (Yue and Unger, 2015). Leaf-level isoprene emission is calculated using the photosynthesis-dependent scheme (Unger et al., 2013), which considers the joint effects of temperature, photosynthetic rate, and carbon dioxide. Stomatal conductance is connected to leaf photosynthesis through the Ball et al. (1987) scheme. The YIBs has joined the intercomparison projection of TRENDY for vegetation models since the year 2020 and showed reasonable performance in most of biospheric parameters (Friedlingstein et al., 2020).

By implementing YIBs into GEOS-Chem, the GEOS-Chem-YIBs (GC-YIBs) model builds the interactions between atmospheric chemistry and land ecosystems (Lei et al., 2020). Within this framework, the YIBs dynamically predicts BVOCs emissions, daily LAI, and stomatal conductance, which are fed into GEOS-Chem to calculate O_3 formation and dry deposition. In turn, the simulated surface O_3 by the chemical model influences stomatal conductance, carbon fluxes and vegetation

growth in the YIBs model through a semi-mechanistic O_3 damage scheme (Sitch et al., 2007; Unger et al., 2020). Previous studies have demonstrated the good performance of GC-YIBs model in simulating the spatiotemporal variations of LAI, O_3 concentrations, and dry deposition velocity against both site-level and satellite-based observations (Gong et al., 2021; Lei et al., 2020; Lei et al., 2022; Lei et al., 2021).

2.2. Land cover change

We select the annual vegetation coverage data from the Land-Use Model Intercomparison Project (LUMIP, https://www.cesm.ucar.edu/projects/CMIP6/ LUMIP/), which has been used to drive global climate models from historical and future simulations (Ge et al., 2022; Lawrence et al., 2016). We convert the LUMIP vegetation types to the YIBs PFTs based on two rules (Table S2). First, the similar species are grouped for the same PFT in YIBs. For example, we aggregate C_3 annual crops, C_3 perennial crops, and C_3 nitrogen-fixing crops in the LUMIP to the C_3 crop in YIBs. Second, the generic forest coverage is downscaled following the observed ratios of different forest types. The forested primary and secondary lands from LUMIP are summed to derive the total tree cover, and then allocated to EBF, ENF, DBF types in YIBs based on their present-day ratios in the same grid from the land cover product of Moderate Resolution Imaging Spectroradiometer (MODIS, https://modis-land.gsfc.nasa.gov/) averaged for 2001–2012.

The national forest inventory (NFI) was initially established in 1950, and has developed into a comprehensive database with technological innovation. The national statistics were derived from the aggregation of provincial data within a five-year cycle, and the estimation of errors was conducted through stratified sampling, providing convincing and authoritative information on vegetation coverage (Zeng, 2015). However, the temporal variation of forest coverage from the LUMIP fails to capture the observed trends during 1989–2018 as indicated by NFI (Fig. 1c). As a result, we reconstruct historical LULCC data by performing a backward extrapolation of LUMIP LULCC from 2014 to 1990 based on the following rules: (1) the growth rate of total tree cover in China is consistent with that from NFI(0.36 % yr^{-1}) during 1990–2014; (2) the spatial pattern of the changes in forest coverage is consistent with that from MODIS version C5 data; (3) the trends of forest and non-forest (excluding crops) areas in each grid are opposite, indicating that the increase of forest area is accompanied by a loss of non-forest types. The rule (3) is applied because observations suggested a simultaneous reduction in shrubland and grassland in the past several decades (Fig. S1).

We do not use the latest version (C6) of MODIS LULCC dataset because it could not capture the afforestation tendency in China (Yue et al., 2021). The MODIS C6 data showed that forest coverage increased from 9.5 % to 10.3 % during 2001–2012, which is significantly different from the 18.2 % to 21.6 % of NFI from 1999 to 2013. Instead, the earlier version (C5) of MODIS LULCC showed a more consistent increase of forest coverage from 16 % in 2001 to 21 % in 2012. However, the MODIS version C5 data span only for 2001–2012. As a result, we reconstruct the long-term LULCC data by adjusting LUMIP so that the updated LULCC matches the spatial pattern of MODIS C5 retrieval (Fig. S1) and the temporal trend of NFI (Fig. 1c). The improved LUMIP shows high (>40 %) forest coverage in southern and northeastern China (Fig. 1a), where the forest area increased steadily over the past three decades (Fig. 1b). The maximum forest expansion is located in central China along the border areas of Shaanxi, Sichuan, Chongqing, and Hubei provinces, consistent with the observations from MODIS version C5 dataset (Fig. S1a). These changes in forest and shrubland area are similar between the earlier (2001−2012) and the recent (2014–2019) periods (Fig. S1). Variations in the whole national (both urban and natural) vegetation cover were considered in the new LULCC version. We compared our LULCC data with the recently reconstructed national LCC data from Yu et al. (2022b) (Fig. S2). Both datasets show consistent spatial distributions with similar hotspots in the southern and northeastern China, achieving a high correlation of 0.87. Furthermore, the correlation coefficient of temporal trends for the two datasets reaches 0.99. The total tree fractions in China calculated with our LULCC data show consistent year-to-year variations with Yu et al. (2022b) (Fig. S2e), though the forest domain is more localized in our product than the latter dataset.

2.3. Sensitivity experiments

We perform a total of 7 sensitivity experiments with the GC-YIBs model (Table 1). These simulations can be divided into two groups. The first group (G1) includes global simulations at 4° × 5° (latitude by longitude) resolution from 2000 to 2019, and the second group (G2) includes nested-grid simulations over Asia with 0.5° × 0.625° resolution during 2014–2019 using the boundary conditions output from the first group. For the G1 group, we design one baseline simulation and three sensitivity runs. The baseline run (G1_BASE) implements interannually varied forcings including meteorological variables, LULCC, and

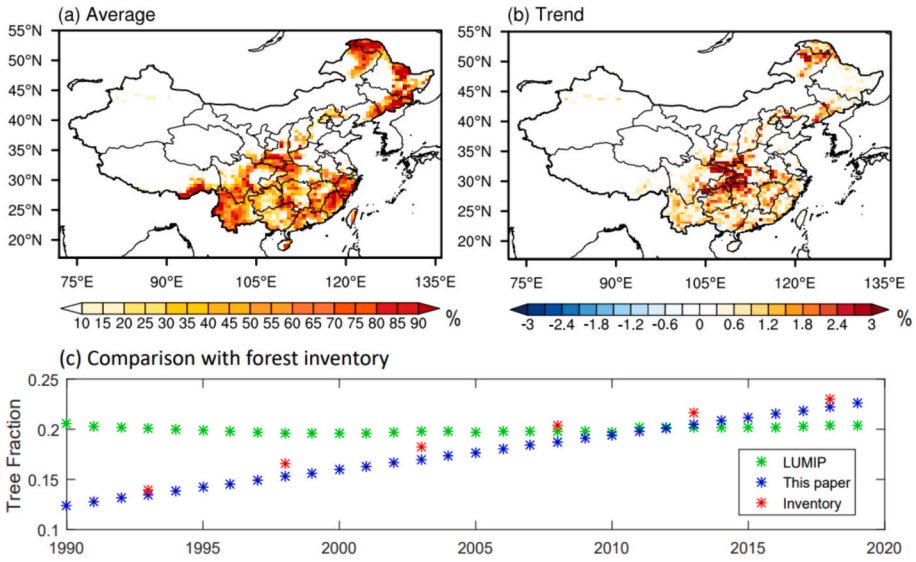

Fig. 1. The spatial distribution of (a) annual average and (b) long-term trend of forest coverage in China, and the (c) comparison of temporal variations with forest inventory from 2000 to 2019.

Table 1
Summary of sensitivity experiments.

Name	Configurations
Global simulations at 4° × 5° for 2000–2019	
G1_BASE	Interannually varied LULCC, meteorology, and anthropogenic emissions
G1_SENS_LULCC	The same as G1_BASE but land cover fixed to 2000
G1_SENS_MET	The same as G1_BASE but meteorology fixed to 2000
G1_SENS_ANTH	The same as G1_BASE but anthropogenic emissions fixed to 2000
Regional simulations in China at 0.5° × 0.625° for 2014–2019	
G2_BASE	Interannually varied LULCC, meteorology, and anthropogenic emissions
G2_SENS_LULCC	The same as G2_BASE but land cover fixed to 2000
G2_SENS_LCISO	The same as G2_BASE but isoprene emissions are input offline

anthropogenic emissions. The other three runs apply the same model configurations as G1_BASE but with fixed meteorology (G1_SENS_MET), LULCC (G1_SENS_LULCC), or anthropogenic emissions (G1_SENS_ANTH) at the year 2000. For the G2 group, we also perform one baseline (G2_BASE) run with year-to-year forcings and one sensitivity simulation with fixed LULCC at 2000. To isolate the contributions of BVOCs emissions to O_3 formation, we conduct an additional run G2_SENS_LCISO with prescribed isoprene emissions output from the G2_BASE.

The differences between baseline (e.g., G1_BASE) and sensitivity (e.g., G1_SENS_LULCC) experiments represent the impacts of the specific disturbance (e.g., LULCC) on O_3 pollution in China. The differences between G2_SENS_LCISO and G2_SENS_LULCC isolate the impacts of LULCC-induced changes in isoprene emissions on surface O_3. In addition to sensitivity experiments, we diagnose the contributions of different processes (e.g., emission, deposition, transport, mixing and convection) to the changes of O_3 concentrations using a mass-balanced approach (Lei et al., 2022). All simulations are spun up for 6 months to reach the equilibrium between emissions and air pollutants.

2.4. Evaluation data and methods

Measurements of surface O_3 are collected from the network of China National Environmental Monitoring Center (CNEMC), which reports hourly surface O_3 concentrations at 1580 sites covering >450 cities. Observational sites with missing values are eliminated, leading to a total of 1564 sites for the model validations. We interpolate the simulated O_3 concentrations to the site locations using a bilinear interpolation approach, and calculate the correlation coefficient (R) and root mean square error (RMSE) against observations as follows:

$$R = \frac{\sum_{i=1}^{n}(M_i - \overline{M})(O_i - \overline{O})}{\sqrt{\sum_{i=1}^{n}(M_i - \overline{M})^2}\sqrt{\sum_{i=1}^{n}(O_i - \overline{O})^2}} \quad (1)$$

$$RMSE = \sqrt{\frac{\sum_{i=1}^{n}(M_i - O_i)^2}{n}} \quad (2)$$

where M_i and O_i are data pairs of simulated and observed O_3 concentrations, respectively.

We also use gridded LAI data form the Global Land Surface Satellite (GLASS) product (Ma and Liang, 2022) developed using the MODIS retrieval. The GLASS LAI gap-fills the original MODIS data with a 0.25° × 0.25° spatial resolution and has been widely used for model validations (Wang et al., 2018; Xie et al., 2019; Yu et al., 2018).

3. Results

3.1. Model evaluations

We compare the simulated 2014–2019 summertime MDA8 O_3 to site-level measurements (Fig. 2). Both the model and observations show the maximum O_3 concentrations in NCP, and the high values in YRD and Sichuan Basin (SCB) regions. The modeled O_3 concentrations range from 24.2 to 93.9 ppbv, similar to the observed range of 22.3–99.5 ppbv for all sites. A high correlation coefficient of 0.82 and low RMSE of 15.2 ppbv are achieved between observations and simulations at 1564 sites, indicating a good performance of GC-YIBs model in capturing the spatial distribution of O_3 pollution in China. For the temporal variation, the model reproduces the day-to-day changes of MDA8 O_3 over northeastern and southeastern China during the summer of 2014–2019 with correlation coefficients of 0.63 and 0.68 in these two regions, respectively (Fig. 2c). Nevertheless, the model on average overestimates MDA8 O_3 by 18 % relative to the observed values. Such overestimation is also reported by other chemical transport models (Dang and Liao, 2019; Gong et al., 2020; Wang et al., 2021) and is possibly caused by the relatively low horizontal resolutions and insufficient observational sites.

The modeled summer LAI is compared to the satellite retrieval from the GLASS product (Fig. 3). Observations show high LAI in northeastern and southern China (Fig. 3a) where most forest locates (Fig. 1a). Simulations in general capture such pattern but with higher LAI by 0.45 m^2 m^{-2} (13.2 %) in the South while lower LAI by 0.78 m^2 m^{-2} (22.5 %) in the Northeast (Fig. 3c). For the period of 2014–2019, the GC-YIBs model predicts increased LAI in southern China (Fig. 3d) though such simulated trend is lower by 0.015 m^2 m^{-2} (31.8 %) than observations (Fig. 3b). For the longer period of 2000–2019, the GC-YIBs model with coarse resolutions also predicts reasonable distribution and temporal trend of LAI in China, though the simulation shows lower magnitude than observations (Fig. S3).

3.2. Impacts of LULCC on surface O_3

LULCC caused large forest growth in southern China (Fig. 1b), leading to the strong enhancement of regional LAI especially over Sichuan, Chongqing, and PRD during 2014–2019 (Fig. 4b). Following these changes, isoprene emissions increase in most of forest regions especially in southern China (Fig. 4c). However, the relative changes of isoprene emissions show the hotspots in NCP (Fig. S4c), where O_3 concentrations are high (Fig. 2b) and the baseline BVOCs are low due to limited forest coverage. Dry deposition velocity in general increases following the changes of LAI with regional maximum enhancement up to 0.02 cm s^{-1} (10.4 %) over the southern and northeastern China (Fig. 4d), indicating an increase of O_3 removal by the forest expansion.

Following the LULCC-induced perturbations in LAI, isoprene emissions, and dry deposition, surface MDA8 O_3 concentrations show heterogeneous changes in China (Fig. 4a). Strong O_3 enhancements up to 6.4 ppbv (6.9 %) are mainly located in the polluted areas such as NCP, YRD, and SCB, where the background O_3 is normally higher than 60 ppbv. The O_3 formation in these regions is usually VOC-limited (Fig. S5) due to the high anthropogenic emissions of NO_x. As a result, the increase of BVOCs from LULCC promotes the regional O_3 pollution. In contrast, the areas with negative changes of O_3 are in general located at rural and remote regions in the South with low background O_3 and/or the NO_x-limited regime (Fig. S5). Particularly, the LULCC decreases in MDA8 O_3 concentration decreases up to 2.69 ppbv (−4.4 %) at the border of Sichuan, Chongqing, and Shaanxi. For these regions, the high forest coverage with large BVOCs emissions and the low emissions of anthropogenic precursors result in the NO_x-sensitive conditions. Consequently, the excessive isoprene will react with O_3 and reduce O_3 concentrations (Fu and Tai, 2015). Furthermore, the high dry deposition by forest contributes to more O_3 removal in these regions. Compared to the mean state, the LULCC causes larger impacts on the O_3 pollution extremes. The

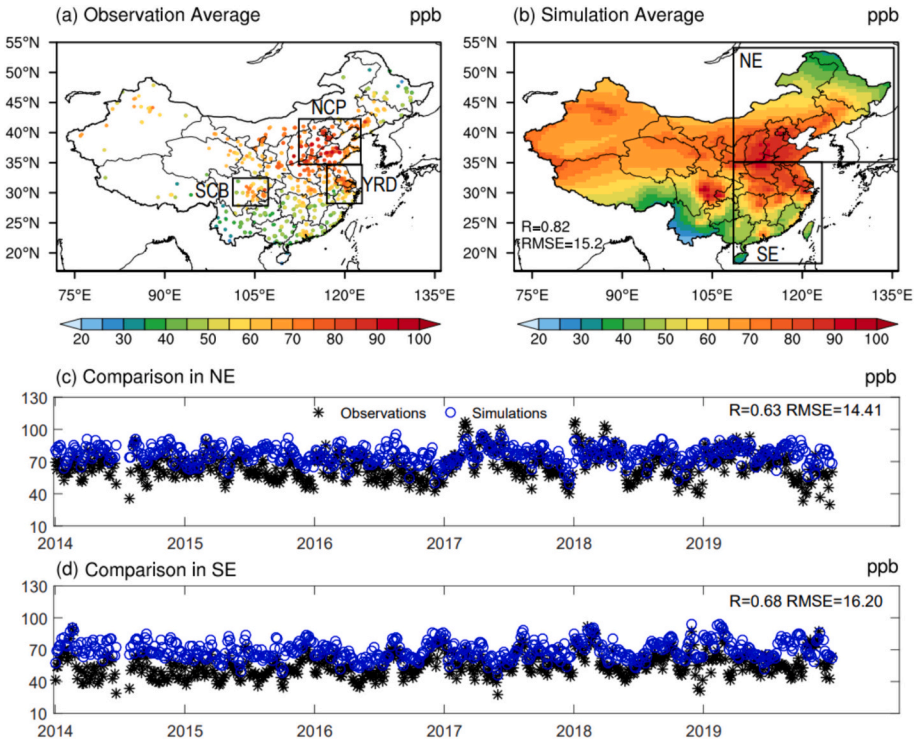

Fig. 2. Evaluations of simulated 2014–2019 summertime surface O_3 from G2_BASE run. Observations (a) from CNEMC network and simulations (b) from GC-YIBs model show similar spatial distribution. Observed and simulated daily concentrations are compared for (c) North China and (d) South China. The (b) spatial and (c-d) temporal correlation coefficients and RMSEs are shown on the panels. The domains of North China Plain (NCP), Yangtze River Delta (YRD), and Sichuan Basin (SCB) are indicated on the map of (a).

LULCC-induced changes in the 95th percentile MDA8 O_3 (Fig. S6b) resemble that in mean O_3 (Fig. 4a) but with more positive values. In addition, considering the climate differences between the northern and southern China, we further added spring and autumn months (April to September) to the time period of study (Fig. S8) and achieved the same conclusions.

We isolate the contributions of LULCC-induced changes in isoprene emissions and dry deposition to O_3 formation (Fig. 5). The increase of isoprene emissions (Fig. 4c) contributes to additional O_3 production by up to 1.5 Kg s^{-1} in SCB (the hotspot in Southwest), and about 0.1–0.5 Kg s^{-1} in NCP, YRD, and PRD (Fig. 5a). However, in other southwestern regions surrounding SCB, the more abundant isoprene emissions inhibit O_3 formation by about −0.1 to −0.5 Kg s^{-1}. As a comparison, the increase of dry deposition (Fig. 4d) causes moderately negative impacts (−0.01 to −0.1 Kg s^{-1}) on O_3 formation (Fig. 5b). In general, the magnitude of O_3 change by isoprene emissions (Fig. 5a) is much larger than that by dry deposition (Fig. 5b), dominating the patterns of LULCC-induced changes in O_3 concentrations (Fig. 4a). On the national scale, the increase of isoprene emissions result in a net O_3 production of 62.0 Kg s^{-1} while the increase of dry deposition causes a net O_3 loss of −23.0 Kg s^{-1} during the summer of 2014–2019. Contributions of other processes including transportation, mixing, and convection were explored as well (Fig. S7). The effects of transportation (Fig. S7a) tend to buffer the changes of air pollutants, thus showing contrary variations to distribution of LULCC-induced ozone changes (Fig. 4a). Influences of mixing (Fig. S7b) and convection (Fig. S7c) caused by LULCC were similar but smaller than that of dry deposition (Fig. 5b).

3.3. Comparison of LULCC impacts with other factors

We compare the contributions of anthropogenic emissions, climate change, and LULCC to the changes of summer MDA8 O_3 concentrations in 2000–2019 (Fig. 6). The national emissions of anthropogenic VOCs and NO_x show increasing trends of 0.09 Tg C yr^{-1} and 0.12 Tg N yr^{-1}, respectively (Fig. S9). The most significant enhancement of emissions is found in NCP, YRD, SCB, and PRD regions, where O_3 pollution events occur frequently (Fig. 2a). Compared to the simulations with fixed anthropogenic emissions at the year 2000, GC-YIBs predicts widespread increase of surface O_3 due to the increased anthropogenic emissions in the past two decades (Fig. 6a). Most of such O_3 enhancement is located in the East and South, with regional hotspots up to 20 ppbv in SCB and YRD.

Temperature and radiation are key factors affecting O_3 production. On the national scale, both temperature and radiation show moderately decreasing trends in the past two decades (Figs. S7c-S7d). Regionally, the two meteorological parameters show heterogeneous patterns. Temperature increases in the East and South but decreases in the Northeast and Southwest (Fig. S10a). Solar radiation decreases in most areas except for NCP (Fig. S10b). The joint increases of temperature and radiation promote surface O_3 up to 3.9 ppbv in NCP (Fig. 6b). In the southern part, the warming effects outweigh the dimming effects, leading to increased surface mean O_3 by 1–3 ppbv. However, in the northern part, the cooling (or the slight warming) and strong dimming together reduces surface mean O_3 by 2–4 ppbv.

The LULCC-induced O_3 changes show consistent spatial patterns between the periods of 2000–2019 and 2014–2019, though the magnitude of changes is lower in the former period in part due to differences in spatial resolution (Fig. 6c and Fig. 4a). In addition, the fast growth of anthropogenic emissions (Fig. S9) provides a more favorable environment for the exacerbation of O_3 pollution in recent years with increased BVOCs emissions from forest expansion. The contribution of LULCC to O_3 concentrations over the past 20 years (Fig. 6c) is much smaller than that by anthropogenic emissions (Fig. 6a), but is comparable to the effects of climate change (Fig. 6b). Regionally, LULCC results in O_3 enhancement of 1–2 ppbv in NCP and the moderate reduction of 0.4–0.8 ppbv in the Southwest. Such pattern resembles the observed O_3 trend

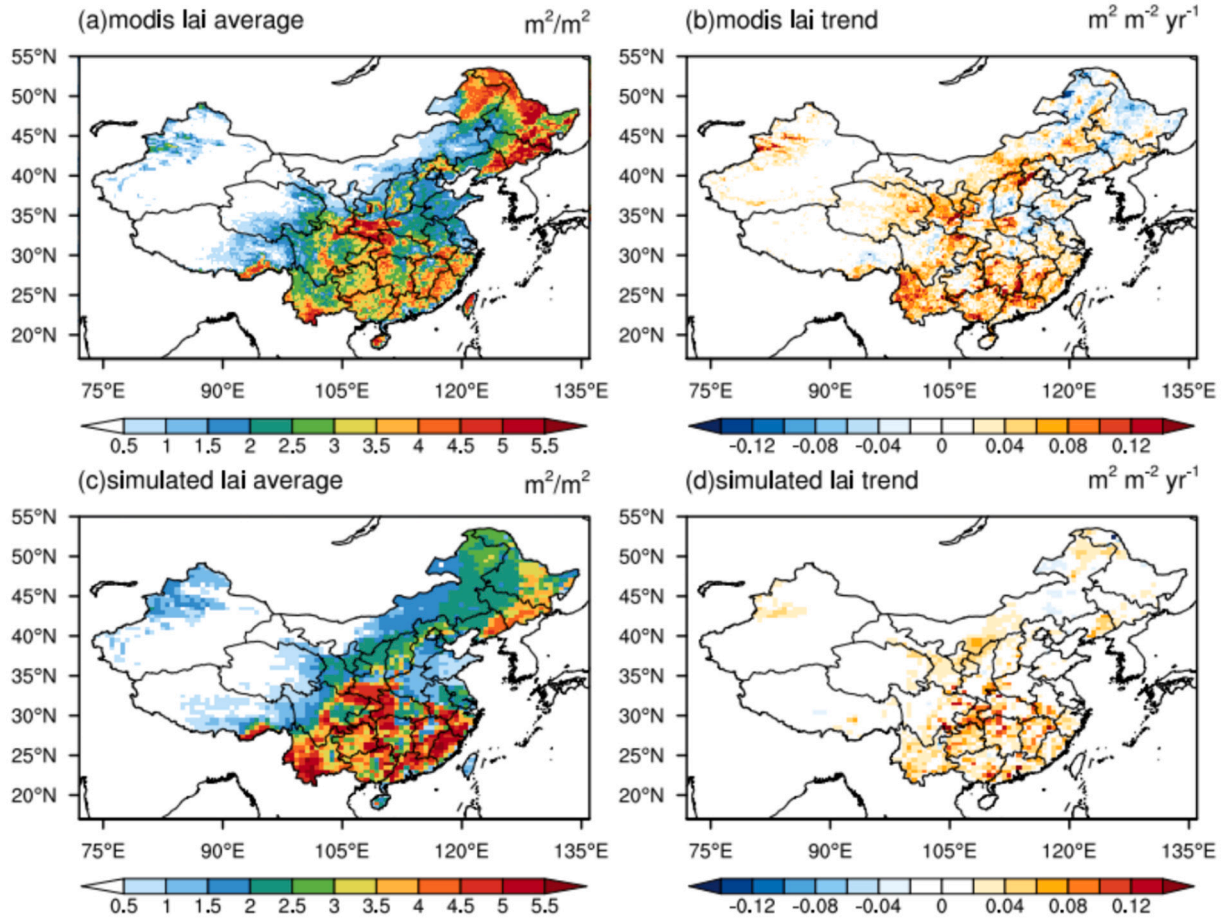

Fig. 3. Evaluations of leaf area index (LAI) from GC-YIBs during 2014–2019. The annual (a, c) average and (b, d) trend of LAI from (a, b) GLASS MODIS data and (c, d) the GC-YIBs simulations are compared.

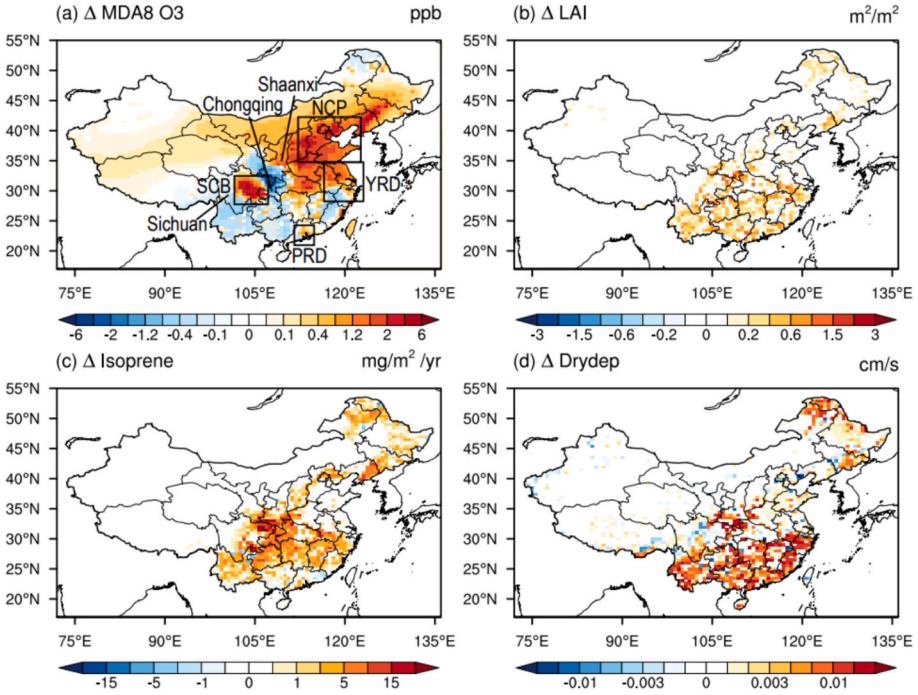

Fig. 4. Simulated changes in summertime surface mean (a) MDA8 O_3 concentrations, (b) LAI, (c) isoprene emissions, and (d) O_3 dry deposition velocity caused by land use and land cover change (LULCC) in 2014–2019.

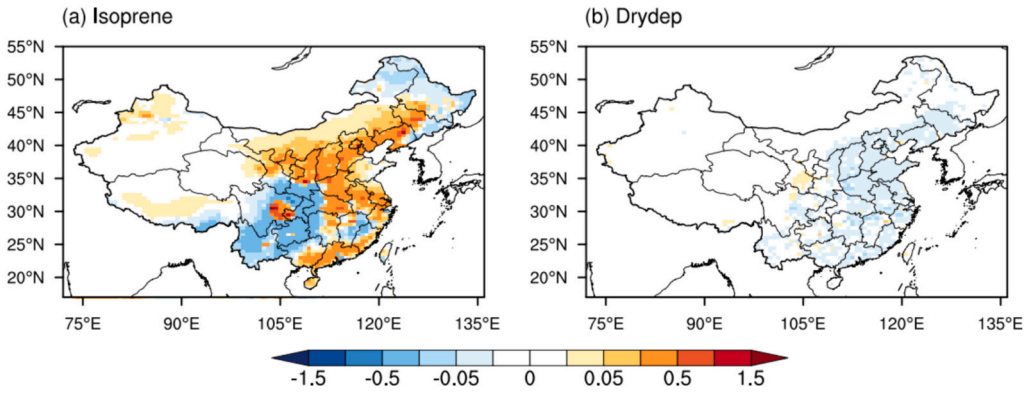

Fig. 5. Attribution of LULCC-induced changes of net O_3 production in China (kg/s) to (a) isoprene emissions and (b) dry deposition during 2014–2019.

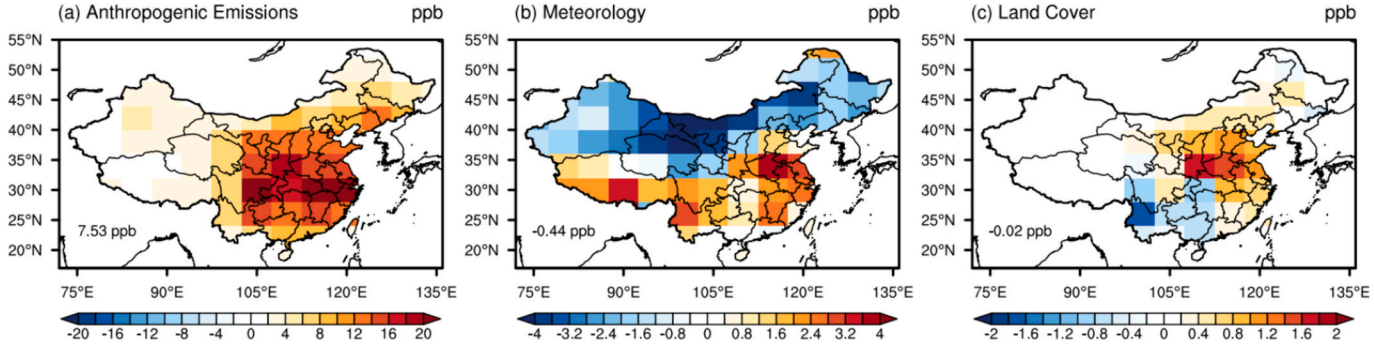

Fig. 6. Changes of summer mean MDA8 O_3 in China due to the changes in (a) anthropogenic emissions, (b) meteorology, and (c) land cover during 2000–2019. The national averages are shown on the panels. Please notice the differences in the color scales.

(Wang et al., 2022), suggesting the important contributions of afforestation to the O_3 pollution in China.

4. Conclusions and discussion

We explored the impacts of LULCC on surface O_3 in China using a coupled chemistry-vegetation model during 2000–2019. Afforestation increases both isoprene emissions and dry deposition in northeastern and southern China. Consequently, surface O_3 shows widespread increase over the northern part with a maximum center of 1–2 ppbv in NCP but the moderate reduction in the South. The LULCC-induced changes in isoprene emissions show stronger impacts than dry deposition in affecting the O_3 budget. The net impact of LULCC on O_3 concentrations is also affected by the background regime of chemical reactions, with positive effects over VOC-limited regions but negative effects in NO_x-limited regions. Although the effects of LULCC are smaller than anthropogenic emissions, forest expansion exacerbates regional O_3 pollution in NCP in the past two decades.

Our results showed large contributions of LULCC to the enhanced O_3 concentrations in NCP, where the absolute changes of isoprene emissions are not significant (Fig. 4c). In contrast, the large enhancement of isoprene emissions by LULCC results in O_3 reductions in the Southwest. Such inconsistency suggests the mismatch of forest expansion and chemical regimes. Afforestation usually occurs in the rural areas with limited anthropogenic emissions (NO_x-limited), leading to O_3 consumption by the additional BVOCs. However, the small increase of BVOCs over the polluted NCP (VOC-limited) provides a more favorable condition for the O_3 enhancement (Fig. S4c). Previous studies showed both opposite and supporting results to our findings. Fu and Tai (2015) and Yu et al. (2022a) found that LULCC led to the decline of O_3 concentrations in NCP due to the increased O_3 dry deposition. In these two studies, dry deposition was diagnosed using the resistance-in-series scheme of Wesely (1989), which had been proved to overestimate dry deposition velocity compared to the Ball-Berry schemes (Cao et al., 2022) used in our study. In addition, the dominant vegetation type in NCP is cropland, whose dry deposition is much smaller than the trees in southern China. Thus, the impacts of dry deposition were likely overestimated in their simulations. On the other hand, Zhang et al. (2020) applied an improved big-leaf model which is more realistic in quantifying the effects of LULCC on the removal of atmospheric pollutants. They found that the influence of biogenic emissions on O_3 budget could not be offset by the O_3 dry deposition in NCP, consistent with our findings.

There are some limitations and uncertainties in our simulations. First, the GC-YIBs model does not consider the interactions between meteorology and vegetation. In addition to the variations in forest coverage and LAI, LULCC modifies the energy balance of land surface and the consequent climatic parameters that further perturb the transport and removal of O_3. Such climatic feedback deserves further investigations using the climate-vegetation-chemistry coupled models. Second, biases may exist in the derived LULCC data for simulations. Currently, the most widely used land use products fail to capture the afforestation tendency in China. For example, the LUMIP data showed limited changes in forest coverage (Fig. 1c) and the long-term land use data by Hurtt et al. (2011) even suggested deforestation in China (Yue et al., 2015). In the light of data limitation, we developed the localized land use data with the adjustment for both spatial distribution and temporal variations, and validated the simulated mean and trend of LAI (Fig. 3) to minimize modeling uncertainties. We expect to use more sophisticated land use data to explore the impacts of LULCC on O_3 pollution in the future studies.

Despite these limitations, our study suggests considerable impacts of LULCC on the O_3 pollution in China over the past two decades. The LULCC-induced O_3 responses are dominated by BVOCs emissions, which

show widespread enhancement in southern China but result in the maximum O_3 increment in NCP. Such inconsistency is attributed to the background chemical regimes that determine the nonlinear responses of surface O_3 to the same enhancement of BVOCs. Although afforestation may increase O_3 level over the polluted regions, the magnitude is much smaller than the enhancement caused by anthropogenic emissions. With the more stringent emission control in the future, surface O_3 pollution is likely alleviated and the chemical regime may shift to be more NO_x-limited. We expect that afforestation may have smaller side effects on surface O_3 pollution in China under a greener climate scenario.

CRediT authorship contribution statement

Yang Cao: Writing – review & editing, Writing – original draft, Software, Methodology, Investigation, Formal analysis, Data curation, Conceptualization. **Xu Yue:** Writing – review & editing, Methodology, Conceptualization. **Hong Liao:** Writing – review & editing. **Xuemei Wang:** Writing – review & editing. **Yadong Lei:** Software, Resources. **Hao Zhou:** Data curation.

Declaration of competing interest

The authors declare that they have no known competing financial interests or personal relationships that could have appeared to influence the work reported in this paper.

Data availability

No data was used for the research described in the article.

Acknowledgments

This work was jointly supported by the National Key Research and Development Program of China (grant no. 2023YFF0805402) and National Natural Science Foundation of China (grant nos. 41975155 and 42205118).

Appendix A. Supplementary data

Supplementary data to this article can be found online at https://doi.org/10.1016/j.scitotenv.2024.174821.

References

Ball, J.T., Woodrow, I.E., Berry, J.A., 1987. A model predicting stomatal conductance and its contribution to the control of photosynthesis under different environmental conditions. Prog. Photosynth. Res. 4, 221–224.

Calfapietra, C., Fares, S., Loreto, F., 2009. Volatile organic compounds from Italian vegetation and their interaction with ozone. Environ. Pollut. 157, 1478–1486. https://doi.org/10.1016/j.envpol.2008.09.048.

Cao, J., Chang, M., Pan, Y., Song, T., Liu, Z., Zhao, H., Zhou, M., Zhang, L., Wang, X., 2022. Assessment and intercomparison of ozone dry deposition schemes over two ecosystems based on Noah-MP in China. Atmos. Environ. 290, 119353 https://doi.org/10.1016/j.atmosenv.2022.119353.

Cao, Y., Yue, X., Liao, H., Yang, Y., Zhu, J., Chen, L., Tian, C., Lei, Y., Zhou, H., Ma, Y., 2021. Ensemble projection of global isoprene emissions by the end of 21st century using CMIP6 models. Atmos. Environ. 267, 118766 https://doi.org/10.1016/j.atmosenv.2021.118766.

Chen, C., Park, T., Wang, X., Piao, S., Xu, B., Chaturvedi, R.K., Fuchs, R., Brovkin, V., Ciais, P., Fensholt, R., Tømmervik, H., Bala, G., Zhu, Z., Nemani, R.R., Myneni, R.B., 2019. China and India lead in greening of the world through land-use management. Nat. Sustain. 2, 122–129. https://doi.org/10.1038/s41893-019-0220-7.

Chen, W.H., Guenther, A.B., Wang, X.M., Chen, Y.H., Gu, D.S., Chang, M., Zhou, S.Z., Wu, L.L., Zhang, Y.Q., 2018. Regional to global biogenic isoprene emission responses to changes in vegetation from 2000 to 2015. J. Geophys. Res. Atmos. 123, 3757–3771. https://doi.org/10.1002/2017jd027934.

Chen, X.K., Jiang, Z., Shen, Y.A., Li, R., Fu, Y.F., Liu, J., Han, H., Liao, H., Cheng, X.G., Jones, D.B.A., Worden, H., Abad, G.G., 2021. Chinese regulations are working-why is surface ozone over industrialized areas still high? Applying lessons from northeast US air quality evolution. Geophys. Res. Lett. 48, e2021GL092816 https://doi.org/10.1029/2021gl092816.

Dang, R., Liao, H., 2019. Radiative forcing and health impact of aerosols and ozone in China as the consequence of clean air actions over 2012–2017. Geophys. Res. Lett. 46, 12511. https://doi.org/10.1029/2019GL084605.

Friedlingstein, P., O'Sullivan, M., Jones, M.W., Andrew, R.M., Hauck, J., Olsen, A., Peters, G.P., Peters, W., Pongratz, J., Sitch, S., Le Quéré, C., Canadell, J.G., Ciais, P., Jackson, R.B., Alin, S., Aragão, L.E.O.C., Arneth, A., Arora, V., Bates, N.R., Becker, M., Benoit-Cattin, A., Bittig, H.C., Bopp, L., Bultan, S., Chandra, N., Chevallier, F., Chini, L.P., Evans, W., Florentie, L., Forster, P.M., Gasser, T., Gehlen, M., Gilfillan, D., Gkritzalis, T., Gregor, L., Gruber, N., Harris, I., Hartung, K., Haverd, V., Houghton, R.A., Ilyina, T., Jain, A.K., Joetzjer, E., Kadono, K., Kato, E., Kitidis, V., Korsbakken, J.I., Landschützer, P., Lefèvre, N., Lenton, A., Lienert, S., Liu, Z., Lombardozzi, D., Marland, G., Metzl, N., Munro, D.R., Nabel, J.E.M.S., Nakaoka, S.I., Niwa, Y., O'Brien, K., Ono, T., Palmer, P.I., Pierrot, D., Poulter, B., Resplandy, L., Robertson, E., Rödenbeck, C., Schwinger, J., Séférian, R., Skjelvan, I., Smith, A.J.P., Sutton, A.J., Tanhua, T., Tans, P.P., Tian, H., Tilbrook, B., van der Werf, G., Vuichard, N., Walker, A.P., Wanninkhof, R., Watson, A.J., Willis, D., Wiltshire, A.J., Yuan, W., Yue, X., Zaehle, S., 2020. Global carbon budget 2020. Earth Syst. Sci. Data. 12, 3269–3340. https://doi.org/10.5194/essd-12-3269-2020.

Fu, Y., Tai, A.P.K., 2015. Impact of climate and land cover changes on tropospheric ozone air quality and public health in East Asia between 1980 and 2010. Atmos. Chem. Phys. 15, 10093–10106. https://doi.org/10.5194/acp-15-10093-2015.

Ge, J., Liu, Q., Zan, B.L., Lin, Z.Q., Lu, S., Qiu, B., Guo, W.D., 2022. Deforestation intensifies daily temperature variability in the northern extratropics. Nat. Commun. 13, 1–15. https://doi.org/10.1038/s41467-022-33622-0.

Gong, C., Lei, Y., Ma, Y., Yue, X., Liao, H., 2020. Ozone–vegetation feedback through dry deposition and isoprene emissions in a global chemistry–carbon–climate model. Atmos. Chem. Phys. 20, 3841–3857. https://doi.org/10.5194/acp-20-3841-2020.

Gong, C., Liao, H., Yue, X., Ma, Y., Lei, Y., 2021. Impacts of ozone-vegetation interactions on ozone pollution episodes in North China and the Yangtze River Delta. Geophys. Res. Lett. 48, e2021GL093814 https://doi.org/10.1029/2021GL093814.

Guenther A., Jiang XY., Heald CL., Sakulyanontvittaya T., Duhl T., Emmons LK., Wang X. 2012. The model of emissions of gases and aerosols from nature version 2.1 (MEGAN2.1): an extended and updated framework for modeling biogenic emissions. Geosci. Model Dev. 5, 1471–1492. doi:https://doi.org/10.5194/gmd-5-1471-2012.

Hoesly, R.M., Smith, S.J., Feng, L., Klimont, Z., Janssens-Maenhout, G., Pitkanen, T., Seibert, J.J., Vu, L., Andres, R.J., Bolt, R.M., Bond, T.C., Dawidowski, L., Kholod, N., Kurokawa, J.I., Li, M., Liu, L., Lu, Z., Moura, M.C.P., O'Rourke, P.R., Zhang, Q., 2018. Historical (1750–2014) anthropogenic emissions of reactive gases and aerosols from the community emissions data system (CEDS). Geosci. Model Dev. 11, 369–408. https://doi.org/10.5194/gmd-11-369-2018.

Huang, T., Zhu, X., Zhong, Q., Yun, X., Meng, W., Li, B., Ma, J., Zeng, E.Y., Tao, S., 2017. Spatial and temporal trends in global emissions of nitrogen oxides from 1960 to 2014. Environ. Sci. Technol. 51, 7992–8000. https://doi.org/10.1021/acs.est.7b02235.

Hudman, R.C., Moore, N.E., Mebust, A.K., Martin, R.V., Russell, A.R., Valin, L.C., Cohen, R.C., 2012. Steps towards a mechanistic model of global soil nitric oxide emissions: implementation and space based-constraints. Atmos. Chem. Phys. 12, 7779–7795. https://doi.org/10.5194/acp-12-7779-2012.

Hurtt, G.C., Chini, L.P., Frolking, S., Betts, R.A., Feddema, J., Fischer, G., Fisk, J.P., Hibbard, K., Houghton, R.A., Janetos, A., Jones, C.D., Kindermann, G., Kinoshita, T., Klein, Goldewijk K., Riahi, K., Shevliakova, E., Smith, S., Stehfest, E., Thomson, A., Thornton, P., van Vuuren, D.P., Wang, Y.P., 2011. Harmonization of land-use scenarios for the period 1500–2100: 600 years of global gridded annual land-use transitions, wood harvest, and resulting secondary lands. Clim. Chang. 109, 117–161. https://doi.org/10.1007/s10584-011-0153-2.

Keller, C.A., Long, M.S., Yantosca, R.M., Da Silva, A.M., Pawson, S., Jacob, D.J., 2014. HEMCO v1.0: a versatile, ESMF-compliant component for calculating emissions in atmospheric models. Geosci. Model Dev. 7, 1409–1417. https://doi.org/10.5194/gmd-7-1409-2014.

Lawrence, D.M., Hurtt, G.C., Arneth, A., Brovkin, V., Calvin, K.V., Jones, A.D., Jones, C. D., Lawrence, P.J., de Noblet-Ducoudre, N., Pongratz, J., Seneviratne, S.I., Shevliakova, E., 2016. The land use model Intercomparison project (LUMIP) contribution to CMIP6: rationale and experimental design. Geosci. Model Dev. 9, 2973–2998. https://doi.org/10.5194/gmd-9-2973-2016.

Lei, Y., Yue, X., Liao, H., Gong, C., Zhang, L., 2020. Implementation of Yale interactive terrestrial biosphere model v1.0 into GEOS-Chem v12.0.0: a tool for biosphere–chemistry interactions. Geosci. Model Dev. 13, 1137–1153. https://doi.org/10.5194/gmd-13-1137-2020.

Lei, Y., Yue, X., Liao, H., Zhang, L., Zhou, H., Tian, C., Gong, C., Ma, Y., Cao, Y., Seco, R., Karl, T., Potosnak, M., 2022. Global perspective of drought impacts on ozone pollution episodes. Environ. Sci. Technol. 56, 3932–3940. https://doi.org/10.1021/acs.est.1c07260.

Lei YD., Yue X., Liao H., Zhang L., Yang Y., Zhou H., Tian CG., Gong C., Ma YMA., Gao L., Cao Y. 2021. Indirect contributions of global fires to surface ozone through ozone-vegetation feedback. Atmos. Chem. Phys. 21, 11531–11543. doi:https://doi.org/10.5194/acp-21-11531-2021.

Li, K., Jacob, D.J., Liao, H., Shen, L., Zhang, Q., Bates, K.H., 2019. Anthropogenic drivers of 2013-2017 trends in summer surface ozone in China. PNAS 116, 422–427. https://doi.org/10.1073/pnas.1812168116.

Li K., Jacob DJ., Shen L., Lu X., De Smedt I., Liao H. 2020. Increases in surface ozone pollution in China from 2013 to 2019: anthropogenic and meteorological influences. Atmos. Chem. Phys. 20, 11423–11433. doi:https://doi.org/10.5194/acp-20-11423-2020.

Li, M., Liu, H., Geng, G.N., Hong, C.P., Liu, F., Song, Y., Tong, D., Zheng, B., Cui, H.Y., Man, H.Y., Zhang, Q., He, K.B., 2017a. Anthropogenic emission inventories in China: a review. Natl. Sci. Rev. 4, 834–866. https://doi.org/10.1093/nsr/nwx150.

Li, M., Zhang, Q., Kurokawa, J., Woo, J.H., He, K.B., Lu, Z.F., Ohara, T., Song, Y., Streets, D.G., Carmichael, G.R., Cheng, Y.F., Hong, C.P., Huo, H., Jiang, X.J., Kang, S. C., Liu, F., Su, H., Zheng, B., 2017b. MIX: a mosaic Asian anthropogenic emission inventory under the international collaboration framework of the MICS-Asia and HTAP. Atmos. Chem. Phys. 17, 935–963. https://doi.org/10.5194/acp-17-935-2017.

Lin, H.P., Jacob, D.J., Lundgren, E.W., Sulprizio, M.P., Keller, C.A., Fritz, T.M., Eastham, S.D., Emmons, L.K., Campbell, P.C., Baker, B., Saylor, R.D., Montuoro, R., 2021. Harmonized emissions component (HEMCO) 3.0 as a versatile emissions component for atmospheric models: application in the GEOS-Chem, NASA GEOS, WRF-GC, CESM2, NOAA GEFS-aerosol, and NOAA UFS models. Geosci. Model Dev. 14, 5487–5506. https://doi.org/10.5194/gmd-14-5487-2021.

Lu, X., Hong, J., Zhang, L., Cooper, O.R., Schultz, M.G., Xu, X., Wang, T., Gao, M., Zhao, Y., Zhang, Y., 2018a. Severe surface ozone pollution in China: a global perspective. Environ. Sci. Technol. Lett. 5, 487–494. https://doi.org/10.1021/acs.estlett.8b00366.

Lu, X., Hong, J.Y., Zhang, L., Cooper, O.R., Schultz, M.G., Xu, X.B., Wang, T., Gao, M., Zhao, Y.H., Zhang, Y.H., 2018b. Severe surface ozone pollution in China: a global perspective. Environ. Sci. Technol. Lett. 5, 487–494. https://doi.org/10.1021/acs.estlett.8b00366.

Lu, X., Zhang, L., Chen, Y.F., Zhou, M., Zheng, B., Li, K., Liu, Y.M., Lin, J.T., Fu, T.M., Zhang, Q., 2019. Exploring 2016-2017 surface ozone pollution over China: source contributions and meteorological influences. Atmos. Chem. Phys. 19, 8339–8361. https://doi.org/10.5194/acp-19-8339-2019.

Ma, H., Liang, S., 2022. Development of the GLASS 250-m leaf area index product (version 6) from MODIS data using the bidirectional LSTM deep learning model. Remote Sens. Environ. 273, 112985 https://doi.org/10.1016/j.rse.2022.112985.

Ma, J., Zhu, S., Wang, S., Wang, P., Chen, J., Zhang, H., 2023. Impacts of land cover changes on biogenic emission and its contribution to ozone and secondary organic aerosol in China. Atmos. Chem. Phys. 23, 4311–4325. https://doi.org/10.5194/acp-23-4311-2023.

Mo, Z.W., Shao, M., Wang, W.J., Liu, Y., Wang, M., Lu, S.H., 2018. Evaluation of biogenic isoprene emissions and their contribution to ozone formation by ground-based measurements in Beijing. China. Sci. Total Environ. 627, 1485–1494. https://doi.org/10.1016/j.scitotenv.2018.01.336.

Monks, P., Archibald, A., Colette, A., Williams, M., 2015. Tropospheric ozone and its precursors from the urban to the global scale from air quality to short-lived climate forcer. Atmos. Chem. Phys. 15, 8889–8973. https://doi.org/10.5194/acp-15-8889-2015.

Park, R.J., Jacob, D.J., Field, B.D., Yantosca, R.M., Chin, M., 2004. Natural and transboundary pollution influences on sulfate-nitrate-ammonium aerosols in the United States: implications for policy. J. Geophys. Res. Atmos. 109, D15204. https://doi.org/10.1029/2003JD004473.

Rienecker, M.M., Suarez, M.J., Gelaro, R., Todling, R., Bacmeister, J., Liu, E., Bosilovich, M.G., Schubert, S.D., Takacs, L., Kim, G.-K., Bloom, S., Chen, J., Collins, D., Conaty, A., Da Silva, A., Gu, W., Joiner, J., Koster, R.D., Lucchesi, R., Molod, A., Owens, T., Pawson, S., Pegion, P., Redder, C.R., Reichle, R., Robertson, F. R., Ruddick, A.G., Sienkiewicz, M., Woollen, J., 2011. MERRA: NASA's modern-era retrospective analysis for research and applications. J. Clim. 24, 3624–3648. https://doi.org/10.1175/jcli-d-11-00015.1.

Sitch, S., Cox, P.M., Collins, W.J., Huntingford, C., 2007. Indirect radiative forcing of climate change through ozone effects on the land-carbon sink. Nature 448, 791–794. https://doi.org/10.1038/nature06059.

Unger, N., Harper, K., Zheng, Y., Kiang, N.Y., Aleinov, I., Arneth, A., Schurgers, G., Amelynck, C., Goldstein, A., Guenther, A., Heinesch, B., Hewitt, C.N., Karl, T., Laffineur, Q., Langford, B., McKinney, K.A., Misztal, P., Potosnak, M., Rinne, J., Pressley, S., Schoon, N., Seraca, D., 2013. Photosynthesis-dependent isoprene emission from leaf to planet in a global carbon-chemistry-climate model. Atmos. Chem. Phys. 13, 10243–10269. https://doi.org/10.5194/acp-13-10243-2013.

Unger, N., Zheng, Y., Yue, X., Harper, K.L., 2020. Mitigation of ozone damage to the world's land ecosystems by source sector. Nat. Clim. Chang. 10, 134.

Vinken, G.C.M., Boersma, K.F., Maasakkers, J.D., Adon, M., Martin, R.V., 2014. Worldwide biogenic soil NOx emissions inferred from OMI NO2 observations. Atmos. Chem. Phys. 14, 10363–10381. https://doi.org/10.5194/acp-14-10363-2014.

Wang, H., Wu, Q.Z., Liu, H.J., Wang, Y.L., Cheng, H.Q., Wang, R.R., Wang, L.N., Xiao, H., Yang, X.C., 2018. Sensitivity of biogenic volatile organic compound emissions to leaf area index and land cover in Beijing. Atmos. Chem. Phys. 18, 9583–9596. https://doi.org/10.5194/acp-18-9583-2018.

Wang L., Tai APK., Tam CY., Sadiq M., Wang P., Cheung KKW. 2020. Impacts of future land use and land cover change on mid-21st-century surface ozone air quality: distinguishing between the biogeophysical and biogeochemical effects. Atmos. Chem. Phys. 20, 11349–11369. doi:https://doi.org/10.5194/acp-20-11349-2020.

Wang, T., Xue, L., Feng, Z., Dai, J., Zhang, Y., Tan, Y., 2022. Ground-level ozone pollution in China: a synthesis of recent findings on influencing factors and impacts. Environ. Res. Lett. 17, 063003 https://doi.org/10.1088/1748-9326/ac69fe.

Wang, W.M., Li, C.H., Shu, J.W., Chen, W., 2019. Changes of vegetation in southern China. China-Earth Sci. 62, 1316–1328. https://doi.org/10.1007/s11430-018-9364-9.

Wang, X., Fu, T.-M., Zhang, L., Cao, H., Zhang, Q., Ma, H., Shen, L., Evans, M.J., Ivatt, P. D., Lu, X., Chen, Y., Zhang, L., Feng, X., Yang, X., Zhu, L., Henze, D.K., 2021. Sensitivities of ozone air pollution in the Beijing–Tianjin–Hebei area to local and upwind precursor emissions using Adjoint modeling. Environ. Sci. Technol. 55, 5752–5762. https://doi.org/10.1021/acs.est.1c00131.

Wang, X.M., Situ, S.P., Guenther, A., Chen, F., Wu, Z.Y., Xia, B.C., Wang, T.J., 2011. Spatiotemporal variability of biogenic terpenoid emissions in Pearl River Delta, China, with high-resolution land-cover and meteorological data. Tellus Ser. B Chem. Phys. Meteorol. 63, 241–254. https://doi.org/10.1111/j.1600-0889.2010.00523.x.

Weng, H., Lin, J., Martin, R., Millet, D.B., Jaeglé, L., Ridley, D., Keller, C., Li, C., Du, M., Meng, J., 2020. Global high-resolution emissions of soil NOx, sea salt aerosols, and biogenic volatile organic compounds. Sci. Data 7, 148. https://doi.org/10.1038/s41597-020-0488-5.

Wesely, M.L., 1989. Parameterization of surface resistances to gaseous dry deposition in regional-scale numerical models. Atmos. Environ. 41, 52–63. https://doi.org/10.1016/0004-6981(89)90153-4.

Xie, X.Y., Li, A.N., Jin, H.A., Tan, J.B., Wang, C.B., Lei, G.B., Zhang, Z.J., Bian, J.H., Nan, X., 2019. Assessment of five satellite-derived LAI datasets for GPP estimations through ecosystem models. Sci. Total Environ. 690, 1120–1130. https://doi.org/10.1016/j.scitotenv.2019.06.516.

Yi, K., Zhao, X., Zheng, Z., Zhao, D., Zeng, Y., 2023. Trends of greening and browning in terrestrial vegetation in China from 2000 to 2020. Ecol. Indic. 154, 110587 https://doi.org/10.1016/j.ecolind.2023.110587.

Yu, J., Zhou, W., Wu, J., Li, X., Liu, S., Wang, R., Liu, L., Jiang, Q., Tie, X., Li, G., 2022a. Impacts of changes in land use and land cover between 2001 and 2018 on summertime O3 formation in North China plain and surrounding areas–a case study. J. Geophys. Res. Atmos. 127, e2021JD035956 https://doi.org/10.1029/2021JD035956.

Yu, T., Sun, R., Xiao, Z.Q., Zhang, Q., Liu, G., Cui, T.X., Wang, J.M., 2018. Estimation of global vegetation productivity from global LAnd surface satellite data. Remote Sens. 10, 327. https://doi.org/10.3390/rs10020327.

Yu, Z., Ciais, P., Piao, S., Houghton, R.A., Lu, C., Tian, H., Agathokleous, E., Kattel, G.R., Sitch, S., Goll, D., Yue, X., Walker, A., Friedlingstein, P., Jain, A.K., Liu, S., Zhou, G., 2022b. Forest expansion dominates China's land carbon sink since 1980. Nat. Commun. 13, 5374. https://doi.org/10.1038/s41467-022-32961-2.

Yue, X., Unger, N., 2015. The Yale interactive terrestrial biosphere model version 1.0: description, evaluation and implementation into NASA GISS ModelE2. Geosci. Model Dev. 8, 2399.

Yue, X., Unger, N., Zheng, Y., 2015. Distinguishing the drivers of trends in land carbon fluxes and plant volatile emissions over the past 3 decades. Atmos. Chem. Phys. 15, 11931–11948. https://doi.org/10.5194/acp-15-11931-2015.

Yue, X., Zhang, T.Y., Shao, C.L., 2021. Afforestation increases ecosystem productivity and carbon storage in China during the 2000s. Agric. For. Meteorol. 296, 108227 https://doi.org/10.1016/j.agrformet.2020.108227.

Zeng, W., 2015. The national forest inventory in China: history - results - international context. For. Ecosyst. 2, 23. https://doi.org/10.1186/s40663-015-0047-2.

Zhai, S.X., Jacob, D.J., Wang, X., Shen, L., Li, K., Zhang, Y.Z., Gui, K., Zhao, T.L., Liao, H., 2019. Fine particulate matter (PM2.5) trends in China, 2013-2018: separating contributions from anthropogenic emissions and meteorology. Atmos. Chem. Phys. 19, 11031–11041. https://doi.org/10.5194/acp-19-11031-2019.

Zhang, R., Cohan, A., Pour, Biazar A., Cohan, D.S., 2017. Source apportionment of biogenic contributions to ozone formation over the United States. Atmos. Environ. 164, 8–19. https://doi.org/10.1016/j.atmosenv.2017.05.044.

Zhang, X.D., Du, J., Zhang, L.M., Huang, T., Gao, H., Mao, X.X., Ma, J.M., 2020. Impact of afforestation on surface ozone in the North China plain during the three-decade period. Agric. For. Meteorol. 287, 107979 https://doi.org/10.1016/j.agrformet.2020.107979.

Zheng, B., Tong, D., Li, M., Liu, F., Hong, C., Geng, G., Li, H., Li, X., Peng, L., Qi, J., Yan, L., Zhang, Y., Zhao, H., Zheng, Y., He, K., Zhang, Q., 2018. Trends in China's anthropogenic emissions since 2010 as the consequence of clean air actions. Atmos. Chem. Phys. 18, 14095–14111. https://doi.org/10.5194/acp-18-14095-2018.